

Lowered Phase Transition Temperature of VO₂(M) via Molybdenum Doping Toward Efficient Aqueous Zinc-Ion Batteries

Selçuk Aydin Sahin, Busra Aydogdu, Gulsah Yaman Uzunoglu, and Recep Yuksel*

Rechargeable aqueous zinc-ion batteries have attracted considerable attention as large-scale energy storage systems owing to their safety, sustainability, and cost-effectiveness. However, their practical application has been hindered by limited energy density, primarily determined by cathode performance. Among transition metal oxides, vanadium dioxide (VO₂) is particularly appealing due to its layered structure, rich polymorphism, and ability to host Zn²⁺ ions reversibly. The thermally driven transition from insulating VO₂(M) to conductive VO₂(R) enhances charge transport through the metal–insulator transition (MIT). In this work, molybdenum doping is employed to lower the MIT temperature of VO₂(M).

Doping reduces the MIT temperature of the VO₂(M) phase to 56.7 °C, resulting in the VO₂(R) phase. Electrochemical measurements reveal that Mo-VO₂(R) cathodes deliver up to ten times higher capacity than the pristine VO₂(M), with 3Mo-VO₂(R) reaching 404.8 mAh g⁻¹ at 0.1 A g⁻¹. These findings demonstrate that Mo doping serves as a practical approach to modify VO₂(M) and decrease the MIT temperature, while improving electrochemical performance. Moreover, the heteroatom doping strategy suggests a promising pathway for developing other VO₂ cathodes for efficient rechargeable batteries, which can leverage the heat dissipated in energy storage systems.

1. Introduction

Rechargeable aqueous zinc-ion batteries (AZIBs) have attracted considerable attention as promising energy storage systems for large-scale applications, owing to their superior safety, environmental sustainability, and cost-effectiveness.^[1–4] This surge in attention can be attributed to several appealing characteristics: 1) the variety of possible electrolytes, encompassing both aqueous and nonaqueous types; 2) the elevated redox potential of Zn (-0.763 V relative to a standard hydrogen electrode), enabling the battery to function in aqueous electrolytes, a feature that is challenging for other battery types; 3) the enhanced safety

and lower toxicity associated with zinc-ion batteries (ZIBs); and 4) the reversibility of Zn plating and stripping. Consequently, a prolonged cycle life can be attained; 5) a greater volumetric energy density (specifically, 5855 mAh cm⁻³ compared to 2061 mAh cm⁻³ for lithium-ion batteries) is achievable due to the high-energy density of Zn and the involvement of two electrons in the electrochemical reactions.^[5,6]

Although substantial strides have been made in enhancing performance at room or low temperatures for large-scale applications, the ability to maintain functionality at high temperatures continues to pose a significant challenge.^[7] The exploration of advanced materials aimed at improving high-temperature performance and ensuring a durable lifespan with a consistent power supply is vital for practical applications.^[8] In addition, the inadequate energy density of batteries has emerged as a critical limitation for real-world applications, primarily due to their cathodes, making the search for high-performance new cathode materials a considerable challenge.^[9] As a fundamental component, the performance enhancement of AZIBs heavily relies on the optimization of cathode materials for stability.^[10] As of now, four primary categories have been identified as cathodes for ZIBs, which include Prussian blue analogs,^[11] manganese oxides,^[12] vanadium-based compounds,^[13] and organics.^[14] Among the various candidates, vanadium oxides are notable for their layered or tunnel-type structures, diverse oxidation states, and substantial theoretical capacity for Zn²⁺ storage.^[13] The straightforward distortion of V-O polyhedrons, along with the diverse valence states of vanadium (ranging from +2 to +5), contributes significantly to the adaptability of the V-O structure in forming composites with various cations, resulting in the production of numerous derivatives.^[15,16] The expansive tunnel and

S. Aydin Sahin, B. Aydogdu, R. Yuksel
Electrochemistry and Electrochemical Technologies
Graduate School of Natural and Applied Sciences
Eskisehir Osmangazi University (ESOGU)
Eskisehir 26040, Türkiye
E-mail: recep.yuksel@ogu.edu.tr

G. Y. Uzunoglu
Department of Chemical Engineering
Istanbul Health and Technology University (ISTUN)
Istanbul 34445, Türkiye

R. Yuksel
Department of Chemistry
Eskisehir Osmangazi University (ESOGU)
Eskisehir 26040, Türkiye

R. Yuksel
Advanced Materials Technologies Application and Research Center (IMATEK)
Eskisehir Osmangazi University (ESOGU)
Eskisehir 26040, Türkiye

 Supporting information for this article is available on the WWW under <https://doi.org/10.1002/batt.202500702>

layered structures of these materials enable the movement of Zn^{2+} ions, resulting in superior rate performance and cycling stability. Nevertheless, despite their potential, vanadium-based cathodes are challenged by issues such as vanadium dissolution, sluggish diffusion rates, and structural instability, which limit their long-term cycling stability and thus restrict their broad utilization.^[13,17]

Specifically, vanadium dioxide (VO_2) presents multiple polymorphs—such as tetragonal $VO_2(A)$,^[18] $VO_2(D)$,^[6] monoclinic $VO_2(M)$, rutile $VO_2(R)$,^[19] metastable monoclinic $VO_2(B)$,^[20] among others—each characterized by unique crystallographic frameworks that affect Zn^{2+} insertion behavior.^[13] VO_2 features a notable theoretical capacity of 323 mAh g⁻¹, derived from the V^{4+}/V^{3+} redox couple within a voltage range of 0.3–1.4 V. However, despite these benefits, the practical use of VO_2 encounters several significant challenges, including low capacity and a limited cycle life. These issues stem from a lack of available active sites, inadequate intrinsic conductivity, and the low diffusion coefficients of Zn^{2+} ions.^[21,22]

The metastable $VO_2(B)$ phase, when subjected to thermal treatment in an inert environment, transforms into the monoclinic $VO_2(M)$ phase.^[23] The latter displays a unique metal-insulator transition (MIT) characteristic, transforming from an insulating monoclinic phase ($VO_2(M)$) to a conductive rutile phase ($VO_2(R)$) at around 68 °C, a phenomenon first documented by Morin.^[24] This phase change is accompanied by a concurrent structural rearrangement, leading to considerable modifications in the crystal structure and a sudden transformation in physical properties.^[25] Historically, this phase transition was elucidated by John R. Goodenough in 1971, utilizing crystal-field theory. As the vertices and edges of the VO_6 octahedron are interconnected, the $VO_2(R)$ octahedron creates a more elaborate network structure, where the octahedral structure of $VO_2(R)$ presents a more sophisticated network arrangement. The lattice constants for $VO_2(R)$ are $a = b = 0.451$ nm and $c = 0.304$ nm, and it is categorized within the $P4_2mm$ space group.^[26,27] The insulating $VO_2(M)$ phase is formed at temperatures lower than 68 °C, attributed to a bandgap that exists between the π^* and d_{\parallel} bonds. In contrast, when temperatures rise above this point, the metallic nature of $VO_2(R)$ is observed, resulting from the partial overlap of the unfilled π^* and d_{\parallel} bands at the Fermi level.^[27] This transition is associated with various alterations in physical properties, such as transmittance, electrical conductivity, and refractive index, rendering it an outstanding functional material.^[19] The heat-induced phase transition from insulating $VO_2(M)$ to conductive $VO_2(R)$ phase takes advantage of the MIT feature to significantly improve charge transfer kinetics and electrical conductivity, thereby resulting in a notable enhancement in specific capacity, energy density, and overall electrochemical performance in aqueous ZIBs.^[21] It is significant to highlight that $VO_2(R)$ demonstrates outstanding chemical and thermal stability, making it ideal for utilization in demanding environments characterized by high temperatures and pressures.^[17] Considering the parasitic side reactions occurring at the cathode/electrolyte interface, the stability of the vanadium oxide-based cathode structure and its compatibility with aqueous electrolytes are vital for efficient battery operation.^[28]

In addition, the limited electronic conductivity and ion exchange at the cathode-electrolyte interface, caused by the loss of active substances and the obstruction of the ion diffusion pathway, hinder the electrolyte pH from attaining a low value in the fully charged state.^[29] In this regard, it is imperative to develop $VO_2(R)$ cathodes for stability, long cycle life, and high-rate capability.

Castro-Pardo et al. reported that the high-temperature phase of VO_2 exhibited markedly superior specific capacity, enhanced current rate capabilities, improved electrical conductivity, and lithium-ion diffusivity in comparison to the insulating low-temperature phase. This paves the way for innovative electrode design, facilitating the manipulation of electrochemical reactions near phase transition temperatures, especially enhancing electrochemical performance at higher temperatures, unlike the existing categories of battery chemistries that suffer from performance degradation at increased temperatures.^[30] Utilizing heat-activated $VO_2(M)$ as a cathode in aqueous ZIBs significantly improves the efficiency of these batteries by leveraging the increased conductivity. In this context, Aydogdu et al. were the first to develop a novel methodology for designing and manufacturing monoclinic vanadium dioxide ($VO_2(M)$) cathodes that are activated by heat, specifically targeting applications in aqueous ZIBs. The utilization of an aqueous electrolyte in ZIBs enabled the effective operation of VO_2 cathodes, demonstrating phase transition and improved electrochemical performance at a temperature that is easily achievable, around 68 °C. The MIT characteristic improved the charge transfer capabilities at the interfaces between the electrode and electrolyte, leading to significant enhancements in specific capacity and energy densities. The fabricated $VO_2(M)$ cathodes experienced a heat-induced transformation to $VO_2(R)$, resulting in an extraordinary increase of 400% in capacity. At a current density of 0.1 A g⁻¹, the $VO_2(R)$ cathodes exhibited a specific capacity of 354.6 mAh g⁻¹, providing an impressive energy density of 461.0 Wh kg⁻¹ for aqueous ZIBs. This remarkable performance was attributed to the sudden change in electrical conductivity that occurs upon the thermal activation of the MIT.^[19]

One effective strategy to optimize the VO_2 cathode materials is through heteroatom doping, which has the potential to modify the electronic structure, reinforce the crystal lattice, and lower the MIT temperature.^[21,25,31–33] Dopants, such as tungsten (W), molybdenum (Mo), and niobium (Nb) can create lattice distortions, change V–V spacing, and provide extra charge carriers, thus enhancing both conductivity and Zn^{2+} diffusion.^[17,25,34] Moreover, the substitution doping of multivalent metal ions can significantly lower the formation energy of cathode materials, thereby effectively preventing the collapse of the crystal structure.^[35] Notably, Mo doping has been shown to increase the electrical conductivity of the $VO_2(B)$ cathode, improve structural stability during cycling, and boost electrochemical kinetics across various energy storage applications.^[25] The rutile R phase surfaces of VO_2 are characterized by instability, leading to a spontaneous phase transition to the monoclinic M1 phase. Stahl et al. demonstrated that the introduction of Mo doping stabilizes the surfaces with a rutile structure at small dopant levels. Both M1 and R surfaces undergo considerable relaxation, with or without doping. Specifically,

the metal–metal distances in the uppermost layers can change by up to 0.4 Å. Consequently, the incorporation of Mo enhances the stability of the rutile surface structure.^[36]

In this study, we report the synthesis of Mo-doped VO₂(M) cathodes with varying Mo content, intended for use in aqueous ZIBs. Our approach aimed to lower the MIT temperature of VO₂(M) to enhance electronic conductivity, while ensuring structural stability during repeated Zn²⁺ insertion and extraction thanks to the VO₂(R) phase. Through the Mo heteroatom doping, the MIT temperature of VO₂(M) was systematically and effectively modified within the range of 56.7–65.1 °C. To explore the possible use of heat-activated Mo-VO₂(M) and (R) phases as cathodes in energy storage systems, we assessed their electrochemical performance in aqueous ZIB cell configurations. The fabricated cells were subjected to testing under two distinct conditions: at room temperature and above the MIT temperature that differentiates the VO₂(M) and VO₂(R) phases. We thoroughly examined the effects of Mo doping on phase composition, MIT characteristics, and Zn²⁺ storage capabilities. Mo-VO₂(R) cathodes demonstrated enhanced specific capacity, along with reduced charge transfer resistance, attributed to their MIT characteristics, leading to superior electrochemical performance. When evaluated against Mo-VO₂(M) counterparts, Mo-VO₂(R) cathodes demonstrated a significant increase in specific capacity and reduced charge transfer resistance, which is linked to their unique MIT characteristics, ultimately leading to improved electrochemical performance.

2. Results and Discussion

In this study, the synthesis of Mo-doped VO₂(M) was conducted by incorporating Mo at four different doping levels relative to V atoms to investigate the influence of Mo doping on the morphology, MIT temperature and electrochemical performance of VO₂(M) and VO₂(R) phases as cathode active materials of aqueous ZIBs. Previous studies on VO₂ modification through heteroatom incorporation generally focused on relatively low to moderate doping concentrations (typically within the 1–10 at% range), as this range is considered optimal for heteroatom doping.^[37] The doping levels of 1.5%, 3%, and 6% were selected in this work to represent controlled substitution regimes. Furthermore, a higher concentration of 12% Mo was intentionally included to probe the substitution threshold of heteroatom-dopant incorporation systematically and to assess the structural tolerance of the VO₂ framework under excessive substitution.

As illustrated in Figure 1a, the pristine VO₂(B) material was synthesized by employing the hydrothermal method with a controlled stoichiometric ratio of V₂O₅ to H₂C₂O₄ at 1:3. After the hydrothermal synthesis, the metastable VO₂(B) phase underwent a transformation into the monoclinic VO₂(M) phase through thermal treatment under argon atmosphere at 700 °C.^[19,38] For heteroatom doping, molybdenum salt was introduced into the precursor solution, yielding Mo-doped VO₂(M) structures with nominal Mo concentrations of 1.5%, 3.0%, 6.0%, and 12.0% at., hereafter denoted as 1.5Mo-VO₂(M), 3Mo-VO₂(M), 6Mo-VO₂(M),

and 12Mo-VO₂(M), respectively. Figure 1a illustrates a schematic representation of the synthesis of Mo-VO₂(M) materials.

The hydrothermal products of VO₂(B) generally display 1D forms, including nanorods or nanobelts, which result from its favored growth along the [010] axis. This favored growth is primarily influenced by factors such as the surface tension and polarity of the aqueous solution.^[8,39] The scanning electron microscopy (SEM) image presented in Figure S1a, Supporting Information illustrates that the synthesized VO₂(B) nanostructures were produced in nanoscale dimensions, specifically as nanobelts. These VO₂(B) nanobelts have lengths ranging from 1 to 2 mm, widths spanning 100 to 200 nm, and thicknesses within the range of 10–50 nm. As shown in the SEM image of the VO₂(B) material containing 6% Mo, namely 6Mo-VO₂(B), there was no significant change in the nanobelt morphology. In addition, Mo-VO₂(B) nanobelts were observed to be quite uniform and in bundles (Figure 1b). Energy dispersive X-ray spectroscopy (EDS) images in Figure 1c reveal that the structure contains V, O, and Mo atoms, and that the Mo atoms are homogeneously distributed throughout the VO₂(B) phase.

Figure 1d,e show the SEM and EDS elemental mapping images of VO₂(M) doped with 6% molybdenum, while the SEM and EDS images of VO₂(M) materials with 1.5% and 3% Mo doping levels are provided in Figure S3 and S4, Supporting Information, respectively. The SEM images of the 1.5Mo-VO₂(M) sample revealed that the nanobelt structures transform into relatively thicker microstructures after heat treatment under the influence of high temperature and heat (Figure S3a, Supporting Information), while the SEM images of the 3Mo-VO₂(M) sample showed that the nanobelt structures form into rounder and coarser structures (Figure S4a, Supporting Information). Similarly, the SEM images of the 6Mo-VO₂(M) sample demonstrated that larger round microstructures formed after heat treatment (Figure 1d). Upon examining the EDS elemental mapping images (Figure 1e, S3b, and S4b, Supporting Information), it becomes evident that the synthesized structures are composed of V, Mo, and O atoms. Additionally, the even distribution of Mo atoms within the structure confirms the successful doping of heteroatoms, thereby facilitating the synthesis of Mo-VO₂(M) structures.

The phase composition and crystallographic structures of the synthesized materials were analyzed using X-ray diffraction (XRD). The XRD patterns are illustrated in Figure 2a. The diffraction pattern of the prepared VO₂(B) (JCPDS card no. 81–2392) reveals distinct peaks at $\approx 2\theta \approx 14.4^\circ$ (001), 25.3° (011), 29.1° (110), 33.8° (200), 36.8° (−112), and 49.8° (020), which are characteristic of the monoclinic layered VO₂(B) structure where VO₆ octahedra are arranged in bilayers separated by van der Waals gaps.^[31] Upon thermal treatment, VO₂(B) experiences a topotactic transformation into the monoclinic VO₂(M) phase (JCPDS card no. 44–0252), exhibiting characteristic reflections at $2\theta \approx 28.0^\circ$ (011), 37.1° (200), 42.3° (210), 55.5° (−222), and 65.0° (−133).^[32,40] The VO₂(M) structure can be viewed as a distorted rutile-type lattice derived from the high-temperature tetragonal rutile VO₂(R) phase (space group P4₂ mnm⁻¹).^[26] In VO₂(M), V–V pairing along the c_R axis and the cooperative tilting of VO₆ octahedra reduce the symmetry to monoclinic (P2₁, c⁻¹), resulting in a bandgap of

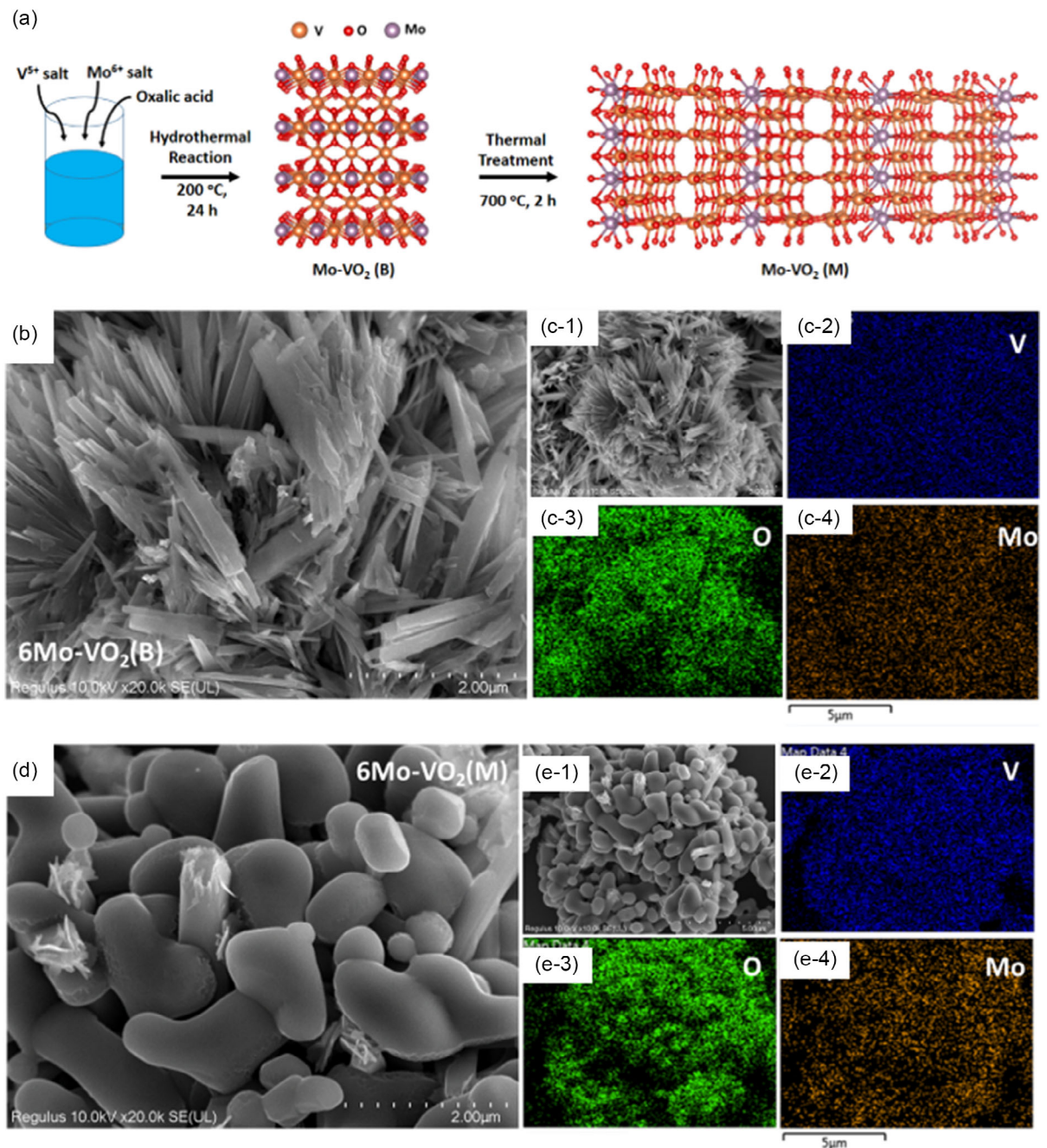


Figure 1. Fabrication of Mo-VO₂(B) and Mo-VO₂(M) materials. a) Schematic representation of Mo-VO₂(B) and Mo-VO₂(M) fabrication steps. b) SEM image and c1–c4) EDS mapping of 6Mo-VO₂(B). d) SEM image and e1–e4) EDS mapping of 6Mo-VO₂(M).

≈0.6 eV and leading to a low-temperature insulating state. Above the MIT temperature, the V–V dimers dissociate, reverting to the rutile VO₂(R) metallic phase.^[32,41] For the Mo-doped VO₂(M) samples (1.5Mo-VO₂(M), 3Mo-VO₂(M), and 6Mo-VO₂(M)), the XRD profiles are identical to that of the undoped VO₂(M), with no observable secondary phases or shifts in peak positions within the limits of instrumental resolution. This suggests that Mo⁶⁺ is integrated into the VO₂ lattice without affecting the long-range crystal symmetry, which is consistent with substitutional doping and charge compensation through the partial oxidation of V⁴⁺.^[42]

The lack of impurity peaks in the diffraction patterns of VO₂(M) materials up to 6% Mo doping level suggests that the synthesized material is of a single phase. This further implies a total conversion of VO₂(B) to the VO₂(M) phase, thus confirming the high purity of the product. Nevertheless, the emergence of new low-intensity peaks (indicated by “**”) was noted in the diffraction pattern of the 12% Mo-doped VO₂(M) sample. This observation is interpreted as the result of excessive Mo heteroatom doping, which alters the structure of VO₂ and leads to the development of a new phase.

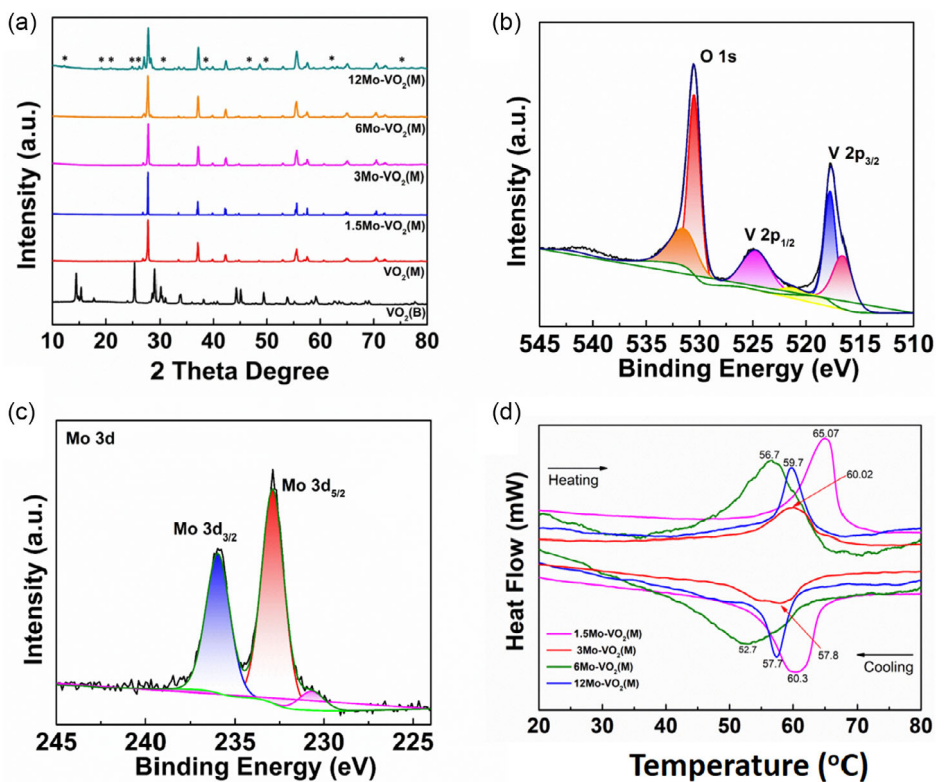


Figure 2. Structural characterization of the Mo-doped $\text{VO}_2(\text{M})$ materials. a) XRD patterns of $\text{Mo}-\text{VO}_2(\text{B})$, $\text{VO}_2(\text{M})$, and $\text{Mo}-\text{VO}_2(\text{M})$ structures. b) High resolution O 1s and V 2p XPS spectra of 6Mo- $\text{VO}_2(\text{M})$. c) High resolution Mo 3d XPS spectrum of 6Mo- $\text{VO}_2(\text{M})$. d) DSC plots of $\text{Mo}-\text{VO}_2(\text{M})$ samples with 1.5%, 3%, 6%, and 12% Mo doping levels.

X-ray photoelectron spectroscopy (XPS) analyses were carried out on the undoped $\text{VO}_2(\text{M})$ and 6Mo- $\text{VO}_2(\text{M})$ samples to identify their surface chemical compositions and valence states of vanadium and molybdenum within the VO_2 lattice. The examination of the high-resolution V 2p and O 1s XPS spectra depicted in Figure 2b indicates that the peaks observed at 523.75 eV and 516.52 eV are associated with V^{+4} 2p_{1/2} and V^{+4} 2p_{3/2}, respectively, verifying the presence of vanadium in the annealed $\text{VO}_2(\text{M})$ crystal at an oxidation state of + 4. A detailed analysis of the V 2p_{3/2} peak at 516.52 eV revealed that the shoulder on the right side comprised two overlapping peaks, which were identified as belonging to the V^{+4} and V^{+5} oxidation states. The occurrence of V^{5+} is linked to the partial oxidation of the particles to V_2O_5 , which takes place solely at the uppermost few nanometers of the surface. This oxidation results from exposure to oxygen following heat treatment or during the storage of the samples in ambient conditions. Given that XRD measurements assess the overall structure of the sample, it is logical that the XRD graph does not exhibit a distinctive peak for the V_2O_5 phase. Given that the V_2O_5 compound represents the highest oxidation state among vanadium oxide derivatives, its presence is frequently observed in XPS analyses.^[8] Furthermore, the oxidation state of vanadium oxides can also be evaluated through the difference in binding energy (ΔE) between the O 1s and V 2p_{3/2} levels. In this study, both the $\text{VO}_2(\text{M})$ and 6Mo- $\text{VO}_2(\text{M})$ synthesized exhibited ΔE (V 2p_{3/2}-O 1s) value of 12.9 eV. This observation is in

strong agreement with the values reported for V^{4+} compounds in existing literature.^[8,38,43] Clear evidence of effective Mo⁶⁺ doping is shown by the presence of the two notable Mo 3d_{5/2} and 3d_{3/2} peaks, located at 231.65 and 234.75 eV, respectively, in the high-resolution Mo 3d XPS spectrum of the 6Mo- $\text{VO}_2(\text{M})$ structure (Figure 2c).^[44] As a result, the XPS spectra associated with 6Mo- VO_2 verified the successful doping of $\text{VO}_2(\text{M})$ phase with Mo⁶⁺ ion.

The differential scanning calorimetry (DSC) curve serves as an effective analytical tool for examining the phase transition temperature of VO_2 . The critical phase transition temperature of the sample during the heating (T_{ch}) or cooling (T_{cc}) process is identified as the apex of the exothermic or endothermic heat flow. T_c represents the critical phase transition temperature of VO_2 , which is calculated as the mean of T_{ch} and T_{cc} . Furthermore, for vanadium dioxide, the area bounded by the exothermic and endothermic peaks indicates the enthalpy changes associated with the VO_2 phase transition, aligning with the latent heat of phase transition.^[42] To gain a deeper insight into the phase transition occurring in the Mo- VO_2 materials, a DSC analysis was carried out on the samples. As shown in the DSC graphs of the Mo-doped $\text{VO}_2(\text{M})$ structures in Figure 2d, the M-R phase transition (MIT) occurred at 64.9, 60.2, 56.7, and 59.7 °C for the 1.5Mo- $\text{VO}_2(\text{M})$, 3Mo- $\text{VO}_2(\text{M})$, 6Mo- $\text{VO}_2(\text{M})$, and 12Mo- $\text{VO}_2(\text{M})$ samples, respectively. The MIT temperature is ≈68 °C for the undoped $\text{VO}_2(\text{M})$.^[19,24,45] Among the synthesized Mo-doped

VO₂(M) structures, the most significant alteration in the temperature at which the MIT property becomes apparent was noted in the 6% Mo-doped VO₂(M) material, providing an 11.3 °C decrease in MIT temperature. For a more extensive analysis, Table S1, Supporting Information summarizes the various heteroatom-doped VO₂ systems that have been reported, including their corresponding MIT temperatures. This comparison evidently indicates that our 6% Mo-doped VO₂ demonstrates one of the most substantial reductions in transition temperature among the systems that have been reported, further underscoring the success of our methodology.

To explore the impact of crystal structure and the Mo doping level in the Mo-VO₂(M) and Mo-VO₂(R) microstructures on their electrochemical performance, the synthesized samples were evaluated as cathode materials for aqueous ZIBs within a voltage range of 0.2–1.5 V at different scan rates ranging from 0.1 to 2.0 mV s⁻¹. Swagelok-type full cells were fabricated, utilizing Zn foil as the anode and a 3.0 M ZnSO₄ aqueous solution as the electrolyte. Comparison of the cyclic voltammetry (CV) profiles of Mo-VO₂(M) cathodes with 1.5%, 3%, and 6% Mo doping levels at a scan rate of 2.0 mV s⁻¹ revealed that the current density of the 1.5Mo-VO₂(M) and 6Mo-VO₂(M) samples is similar to each other and greater than that of the 3Mo-VO₂(M) sample (Figure 3a). Moreover, the enclosed area of the CV curves increased sequentially from 3Mo-VO₂(M) to 6Mo-VO₂(M) and then to 1.5Mo-VO₂(M), with the values for 6Mo-VO₂(M) and 1.5Mo-VO₂(M) being nearly identical. The CV curves associated with the Mo-VO₂(M) cathodes with Mo doping concentrations of 1.5%, 3%, and 6% demonstrated analogous redox behaviors at all scan rates, showing an increase in current density in relation to the CV scan rates as demonstrated in Figure S5a, S6a, and S7, Supporting Information, respectively. It was noted that as the scan rate increases, the oxidation peaks tend to shift toward higher voltage values, while the reduction peaks shift toward lower voltage values. The redox peaks seen in the CV profiles of all Mo-doped VO₂(M) samples were consistent with the characteristic peaks of pure VO₂(M),^[19] exhibiting two distinct oxidation peaks accompanied by two corresponding reduction peaks. These characteristics suggest a stepwise Zn²⁺ intercalation/deintercalation mechanism taking place within the crystal frameworks of these cathode materials.

The electrochemical measurements with Mo-doped VO₂(R) cathodes were performed at 70 °C, a temperature exceeding the threshold at which the MIT characteristic is observed.^[46] It is noteworthy to mention that, although Mo-doped VO₂ samples demonstrate the MIT feature at lower temperatures (Figure 2d), the analysis temperature was kept constant at 70 °C for fair comparison among all samples. Figure 3c illustrates the CV measurements at a scan rate of 2.0 mV s⁻¹ for VO₂(R) cathodes with different levels of Mo doping. As shown in Figure 3c, the CV profiles of Mo-doped VO₂(R) cathodes exhibited more than a 10-fold increase in current density compared with the Mo-VO₂(M) electrodes, a result attributed to the tetragonal rutile structure. Interestingly, unlike the trend observed for Mo doping in the VO₂(M) phase, the 3% Mo-doped VO₂(R) sample delivered the highest current response among the rutile-phase cathodes.

The corresponding CV curves of the 1.5, 3, and 6Mo-VO₂(R) cathodes at various scan rates from 0.1 to 2 mV s⁻¹ are provided in Figure 3e, S5b, and S6b, Supporting Information, respectively. This enhanced electrochemical activity stems from the M-R phase transition, which significantly increases the electronic conductivity of the VO₂ lattice while simultaneously facilitating faster Zn²⁺ ion transport. The combination of improved charge transfer and greater structural adaptability afforded by the MIT transition underpins the superior performance of the Mo-VO₂(R) cathodes.^[19,34]

For a comprehensive evaluation of the electrochemical characteristics of Mo-doped VO₂(M) cathodes, galvanostatic charge and discharge (GCD) measurements of the aqueous ZIBs with Mo-doped VO₂(M) cathodes were conducted within a voltage range of 0.2–1.5 V. These GCD measurements of the aqueous ZIBs were performed at 25 °C in order to observe the battery performance of the Mo-doped VO₂(M) cathodes without MIT characteristic. As shown in the GCD profiles at a current density of 0.1 A g⁻¹ (Figure 3b), the 1.5Mo-VO₂(M), 3Mo-VO₂(M), and 6Mo-VO₂(M) cathodes delivered specific capacities (C_{sp}) of 25, 18, and 44 mAh g⁻¹, respectively. Among these, the 6Mo-VO₂(M) cathode exhibited the highest capacity, suggesting that an optimal level of Mo incorporation enhances electronic conductivity and Zn²⁺ insertion kinetics, whereas insufficient or excessive doping may limit active site utilization and reduce overall performance.^[21] GCD measurements for the assembled aqueous ZIB devices were carried out across a wide current density range (0.1–5 A g⁻¹), with the corresponding GCD curves for Mo-VO₂(M) cathodes shown in Figure S11a, S12a, and S13, Supporting Information. All three Mo doping concentrations in the VO₂(M) phase exhibited stable cycling behavior and preserved a noticeable fraction of their capacity at elevated current densities, reflecting good rate capability. However, the specific capacities remain modest. While the doping of Mo heteroatoms has led to an enhanced rate capability in Mo-VO₂(M) materials, the limited conductivity and less favorable Zn²⁺ diffusion pathways in the Mo-doped VO₂(M) lattice continue to restrict the overall capacity.

GCD measurements were also performed to investigate the MIT between the monoclinic VO₂(M) and rutile VO₂(R) phases at 70 °C, and to analyze its effect on the electrochemical performance of Mo-doped VO₂(R) cathodes. These measurements were conducted under the same voltage window and current densities as those applied to the Mo-doped VO₂(M) cathodes. The transition to the VO₂(R) phase, as depicted in Figure 3d, produced a notable increase in specific capacity (C_{sp}) values at 0.1 A g⁻¹. This enhancement underscores the critical role of the Mo-VO₂(R) framework in facilitating Zn²⁺ storage and boosting electrochemical performance. The rutile structure provides a more open lattice and higher electronic conductivity due to electron delocalization across V-V chains, which together promote faster ion diffusion and more efficient charge transfer. Such behavior is in good agreement with earlier studies, reporting that the MIT transition significantly improves both charge transport and structural adaptability in VO₂-based cathodes.^[19,25,47] The 1.5Mo-, 3Mo-, and 6Mo-VO₂(R) cathodes exhibited specific capacities of 359.0, 404.9, and 342.5 mAh g⁻¹ at a current density of

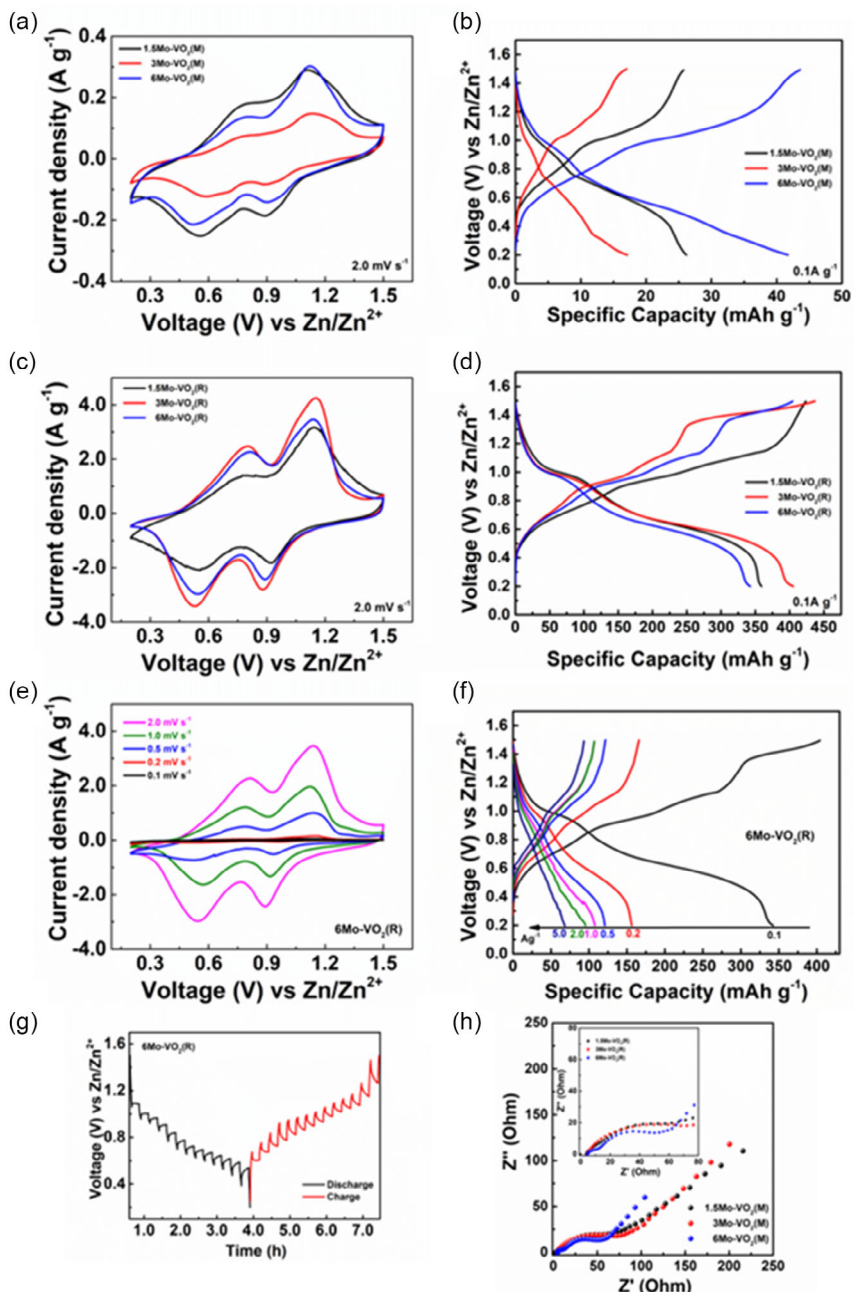


Figure 3. The electrochemical performance of the Mo-doped $\text{VO}_2(\text{M})$ materials. Comparison of the aqueous ZIBs with Mo-doped $\text{VO}_2(\text{M})$ cathodes: a) CV curves at 2.0 mV s^{-1} and b) GCD curves at 0.1 Ag^{-1} . Comparison of the aqueous ZIBs with Mo-doped $\text{VO}_2(\text{R})$ cathodes: c) CV curves at 2.0 mV s^{-1} and d) GCD curves at 0.1 A g^{-1} . The aqueous ZIBs with $6\text{Mo-VO}_2(\text{R})$; e) CV curves at scan rates spanning from 0.1 to 2.0 mV s^{-1} ; f) GCD curves at different current densities from 0.1 to 5 Ag^{-1} ; and g) GITT curves. h) Nyquist plots of the Mo- $\text{VO}_2(\text{M})$ cathodes (Inset: the Mo- $\text{VO}_2(\text{R})$ cathodes).

0.1 A g^{-1} , respectively. Compared with their $\text{VO}_2(\text{M})$ counterparts, these values represent significant enhancements, with 1.5%, 3%, and 6% Mo dopant concentrations showing a \approx 14-, 22-, and 7-fold increase in specific capacity, respectively (Figures S14, Supporting Information). This situation arises from the ability of Mo-doped VO_2 cathodes to perform electrochemical charge transfer more efficiently, as the reduction in charge transfer resistance during the MIT between the M phase and R phase facilitates this process. The individual GCD profile of the $6\text{Mo-VO}_2(\text{M})$

cathode at various current densities spanning from 0.1 to 5 Ag^{-1} is presented in Figure 3f. Accordingly, the $6\text{Mo-VO}_2(\text{R})$ cathode sustained capacities of 107.6, 95.3, and 67.2 mAh g^{-1} at current densities of 1.0, 2.0, and 5.0 Ag^{-1} , respectively. The GCD profiles of $1.5\text{Mo-VO}_2(\text{R})$ and $3\text{Mo-VO}_2(\text{R})$ are also provided in Figure S11b and S12b, Supporting Information, respectively. These findings highlight the advantages of exploiting the $\text{VO}_2(\text{R})$ phase for achieving higher capacity and better rate performance in aqueous ZIBs.

Galvanostatic intermittent titration technique (GITT) analyses were performed to probe further the electrochemical behavior of the 6Mo-VO₂(M) and 6Mo-VO₂(R) cathodes. For the monoclinic 6Mo-VO₂(M) sample, the test involved applying a current density of 0.1 Ag⁻¹ for 3 min, followed by a 12 min relaxation period. In contrast, the rutile 6Mo-VO₂(R) cathode was evaluated under a higher current density of 0.3 Ag⁻¹ with the same pulse-rest protocol. The corresponding voltage-time profiles for 6Mo-VO₂(M) and 6Mo-VO₂(R) are presented in Figure S15a and 3, Supporting Information, while the voltage-capacity relationships are shown in Figure S15b,c, Supporting Information. Finally, the Zn²⁺ ion diffusion coefficients, calculated from GITT graphs, are presented in Figure S15d, Supporting Information. It was noted that the diffusion coefficient of Zn²⁺ ions rises after the transition from the VO₂(M) phase to the VO₂(R) phase. To sum up, consistent with the GCD data, the GITT results confirm that the VO₂(R) phase delivers significantly higher specific capacity compared to its monoclinic counterpart.

The ZIB cells with the Mo-doped VO₂ cathodes were evaluated using the electrochemical impedance spectroscopy (EIS) at distinct bias voltages, covering a frequency range from 100 to 10 mHz. The corresponding comparative Nyquist plots are illustrated in Figure 3h. Each impedance spectrum features a depressed semicircle at high frequencies, followed by a sloping line in the low-frequency range. The depressed semicircle is associated with charge-transfer impedance (R_{ct}), whereas the sloped line ($\approx 45^\circ$) is indicative of Warburg impedance (R_w), which is linked to the semi-infinite diffusion of Zn²⁺ ions into the electrode-electrolyte interface.^[48,49] Our EIS analysis revealed that the R_{ct} values for Mo-VO₂(M) cathodes, ranging from 180 to 220 Ω (Figure S16, Supporting Information), were comparable to those of pristine VO₂(M). Following the M-R phase transition, R_{ct} decreased markedly to $\approx 60 \Omega$ (with the 6Mo-VO₂(R) cathode), reflecting enhanced electronic conductivity and faster Zn²⁺ transport within the VO₂(R) lattice, which correlates with the observed increase in capacity. Collectively, the GCD, GITT, and EIS data consistently demonstrate that the improved electrochemical performance is strongly correlated with the MIT-driven transition to the rutile VO₂(R) phase, while Mo doping alone has a limited impact on the monoclinic VO₂(M) structure.

Consistent with the CV results, Mo-VO₂(R) materials demonstrated a significant change in C_{sp} due to the MIT feature. The C_{sp} values obtained from GCD measurements at various current densities are shown in Figure 4a,b. Overall, the specific capacities of Mo-doped VO₂(R) cathodes were greater than those of Mo-VO₂(M) cathodes. In addition, Mo-doped VO₂(R) cathodes exhibited a high specific capacity when subjected to low current densities. Measurements of capacity retention for Mo-doped VO₂(M) cathode materials were performed at a current density of 2.0 Ag⁻¹. Results for the measurements of Mo-doped VO₂(M) cathodes with different ratios are depicted in Figure 4c. Impressively, the specific capacity of 6Mo-VO₂(M) under a current density of 2 Ag⁻¹ demonstrated a continuously increasing capacity up to the 6000th cycle, after which its capacity gradually kept increasing toward the 10000th cycle. Although the prepared

cathodes exhibited low capacity during the initial cycles, their capacity gradually increased with the number of cycles. This gradual capacity increase was attributed to a progressive activation process rather than parasitic side reactions. During prolonged cycling, previously less-accessible active regions become electrochemically engaged through gradual structural relaxation and improved electrolyte penetration, while Mo incorporation likely enhances lattice flexibility. Similar activation-induced behavior has been reported in other doped vanadium-based cathodes, supporting that this anomalous trend originates from delayed utilization of active sites rather than instability.^[21,50-58] Validating this interpretation, recent findings by Zhang et al. (2025) revealed that Mo doping not only accelerates electrochemical kinetics but also reduces structural dissolution in VO₂ cathodes, thereby extending their cycling lifespan.^[21]

The analysis of the cycle life and capacity retention of Mo-doped VO₂(R) cathodes was also conducted at a current density of 2.0 Ag⁻¹. Measurement results for Mo-doped VO₂(R) cathodes at various ratios are presented in Figure 4d. Accordingly, the 1.5Mo-VO₂(R) cathodes achieved the highest capacity value of 134.9 mAh g⁻¹ during the 126th cycle, but exhibited a declining capacity trend in subsequent cycles. The 3Mo-VO₂(R) material reached its peak specific capacity of 219.8 mAh g⁻¹ in the 77th cycle, followed by a decreasing trend thereafter. In contrast, the 6Mo-VO₂(R) material attained its maximum specific capacity of 115.2 mAh g⁻¹ in the 103rd cycle, after which its capacity diminished in the following cycles.

To further elucidate the structural evolution of the cathode during Zn²⁺ insertion and extraction, ex situ XRD measurements were conducted at various charge-discharge states for the 3Mo-VO₂(M) electrode (Figure 4e). Notably, the characteristic diffraction peak located near 28° exhibited a gradual and reversible shift toward lower angles upon discharge and returned toward higher angles upon charging. This shift reflects a variation in the interplanar spacing induced by Zn²⁺ intercalation and deintercalation. Specifically, the blue- and redshift behavior of the Mo-VO₂(M) reflections confirms that Zn²⁺ intercalation expands the lattice, while Zn²⁺ deintercalation contracts it back toward its original configuration. The reversible change in peak position demonstrates that the host structure can accommodate repeated Zn²⁺ insertion without irreversible phase degradation, further validating an intercalation-dominated storage mechanism rather than surface-limited capacitive behavior.^[59]

The differences in electrochemical performance noted between Mo-VO₂(M) and Mo-VO₂(R) materials are intricately linked to their fundamental crystal structures. A schematic illustrating the MIT from VO₂(M) to Mo-VO₂(R) is presented in Figure 4f. Understanding the effects of Mo doping in Mo-VO₂(M) material is important in the context of application of this material as an electrode for rechargeable batteries. Future studies incorporating density functional theory (DFT) calculations to elucidate the mechanism underlying the phase transition^[37,60-62] and in situ characterizations, for example, Raman, XPS,^[21] and XRD,^[19] will be valuable to further clarify the thermodynamic and kinetic impact of Mo doping on VO₂ phase transition.

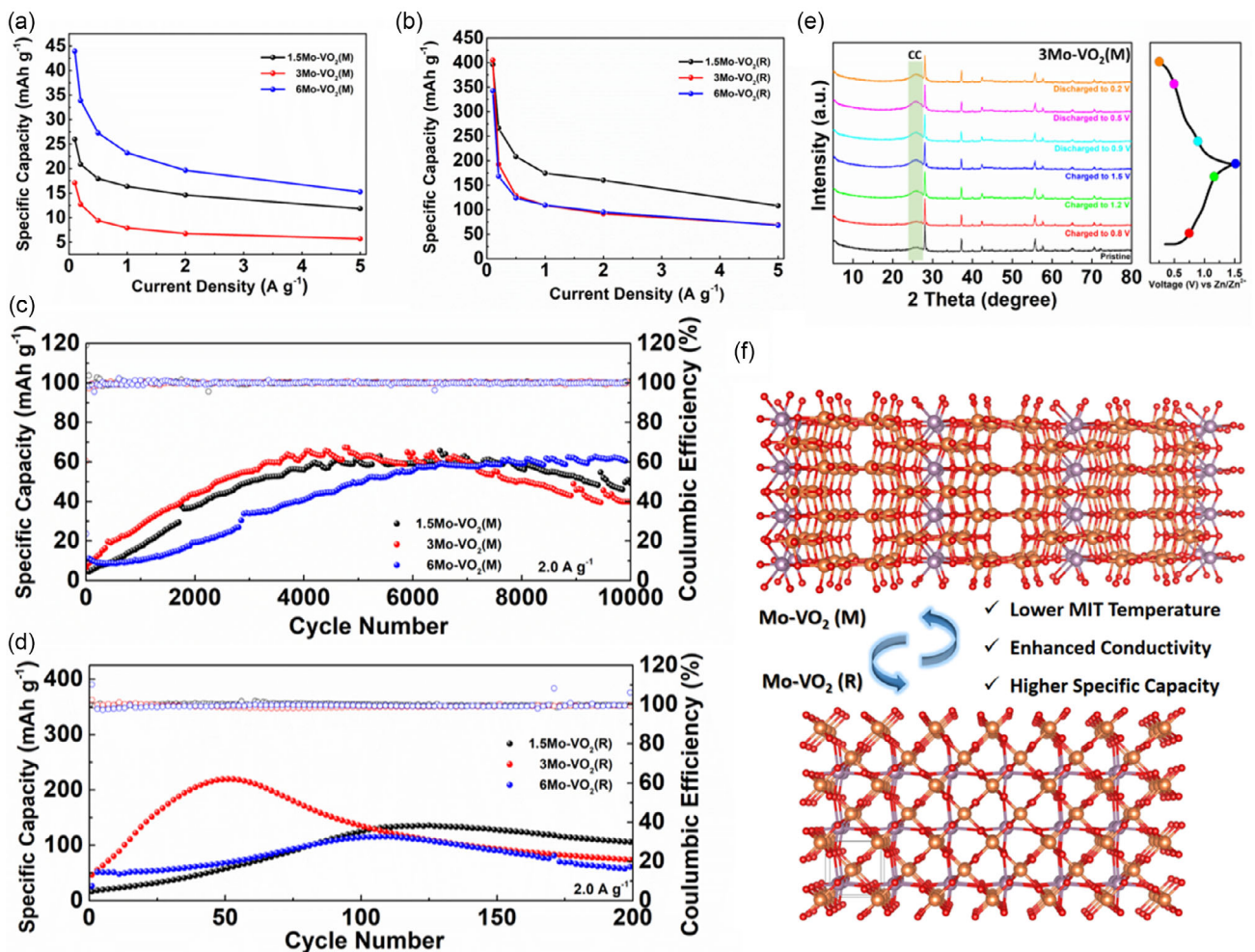


Figure 4. Specific capacities of ZIB devices utilizing a) Mo-VO₂(M) and b) Mo-VO₂(R) cathodes across different current densities. The capacity retention of c) Mo-VO₂(M) and d) Mo-VO₂(R) cathodes at a current density of 2.0 A g⁻¹. e) Ex situ XRD results of the 3Mo-VO₂(M) cathodes. f) Schematic illustration of MIT behavior between Mo-VO₂(M) and Mo-VO₂(R) materials.

3. Conclusion

In this study, to enable the MIT property of VO₂(M) materials to occur at lower temperatures, molybdenum was utilized for heteroatom doping. For this purpose, Mo-VO₂(B) materials with various Mo doping levels were initially synthesized using the scalable hydrothermal method, and then it was irreversibly converted to the stable monoclinic Mo-doped VO₂ phase, namely Mo-VO₂(M), through thermal treatment. MIT behavior was observed between the phases of VO₂(M) and VO₂(R) at lower temperatures due to the Mo doping. Our findings indicated that the 6Mo-VO₂(M) material achieved the most significant reduction in MIT temperature, occurring at 56.7 °C. In addition, our study revealed that Mo-doped VO₂(R) cathodes possess a greater specific capacity (\approx 10-fold) than their Mo-doped VO₂(M) counterparts. Among the Mo-VO₂(R) materials, the 3Mo-VO₂(R) composition demonstrated the highest specific capacity of 404.8 mAh g⁻¹ at a current density of 0.1 A g⁻¹, which corresponds to an impressive gravimetric energy density of 445.3 Wh kg⁻¹. In contrast,

Mo-doped VO₂(M) exhibits comparatively lower capacity, reflecting the limitations of its insulating monoclinic framework, where restricted electronic conductivity and less favorable ion pathways hinder Zn²⁺ storage. Overall, the enhanced capacity of Mo-doped VO₂(R) highlights the pivotal role of the MIT transition in improving electronic conductivity, ion transport, and Zn²⁺ storage capability in aqueous ZIBs. These results indicate that Mo doping serves as a viable tool for modifying VO₂(M) to achieve a reduction in MIT temperature, thereby facilitating the adaptation to thermal fluctuations in the external environment and broadening the potential applications of ZIBs. Furthermore, this modification enhances the performance of ZIBs under varying thermal conditions. The Mo doping strategy proposed here also presents an encouraging pathway for developing other high-energy and stable cathodes for AZIBs. These results highlight the potential of heat-activated VO₂ as a high-performance cathode material, providing valuable insights into phase engineering through heteroatom doping for the rational development of advanced electrochemical energy storage systems.

Acknowledgements

This work was supported by the Scientific and Technological Research Council of Türkiye (TUBITAK) under the grant number 221M072 and Eskisehir Osmangazi University Scientific Research Projects Coordination Unit (grant no: FYL-2023–2740).

Conflict of Interest

The authors declare no conflict of interest.

Author Contributions

Selay Aydin Sahin: data curation (equal), formal analysis (equal).
Busra Aydogdu: data curation (equal), formal analysis (equal).
Gulsah Yaman Uzunoglu: conceptualization (supporting), writing—original draft (lead), writing—review & editing (supporting).
Recep Yuksel: conceptualization (lead), data curation (supporting), formal analysis (supporting), funding acquisition (lead), investigation (lead), methodology (lead), project administration (lead), resources (lead), supervision (lead), validation (lead), visualization (lead), writing—original draft (supporting), writing—review & editing (lead). **Selay Aydin Sahin and Busra Aydogdu** contributed equally to this work.

Data Availability Statement

The data that support the findings of this study are available from the corresponding author upon reasonable request.

Keywords: aqueous Zn-ion batteries • cathodes • energy storage • metal–insulator transition • vanadium dioxide

- [1] Y. Liang, H. Dong, D. Aurbach, Y. Yao, *Nat. Energy* **2020**, *5*, 646.
- [2] Z. Pan, X. Liu, J. Yang, X. Li, Z. Liu, X. J. Loh, J. Wang, *Adv. Energy Mater.* **2021**, *11*, 2100608.
- [3] W. Chen, Y. Wang, F. Wang, Z. Zhang, W. Li, G. Fang, F. Wang, *Adv. Mater.* **2024**, *36*, 2411802.
- [4] G. Y. Uzunoglu, R. Yuksel, *Small* **2025**, *21*, 2411478.
- [5] J. Ming, J. Guo, C. Xia, W. Wang, H. N. Alshareef, *Mater. Sci. Eng.: R: Rep.* **2019**, *135*, 58.
- [6] R. Yuksel, *Adv. Sustainable Syst.* **2024**, *8*, 2400396.
- [7] Q. Wei, T. Huang, X. Huang, B. Wang, Y. Jiang, D. Tang, D. L. Peng, B. Dunn, L. Mai, *Interdisc. Mater.* **2023**, *2*, 434.
- [8] X. Wu, M. Tang, L. Yuan, J. Li, L. Qi, X. Weng, C. Gu, M. Bi, *J. Alloys Compd.* **2025**, *1014*, 178529.
- [9] B. Yong, D. Ma, Y. Wang, H. Mi, C. He, P. Zhang, *Adv. Energy Mater.* **2020**, *10*, 2002354.
- [10] Y. Gan, C. Wang, J. Li, J. Zheng, Z. Wu, L. Lv, P. Liang, H. Wan, J. Zhang, H. Wang, *Front. Chem.* **2022**, *9*, 2021.
- [11] J. Liu, Z. Shen, C.-Z. Lu, *J. Mater. Chem. A* **2024**, *12*, 2647.
- [12] T. Xiong, Z. G. Yu, H. Wu, Y. Du, Q. Xie, J. Chen, Y.-W. Zhang, S. J. Pennycook, W. S. V. Lee, J. Xue, *Adv. Energy Mater.* **2019**, *9*, 1803815.
- [13] K. Zhu, W. Yang, *Acc. Chem. Res.* **2024**, *57*, 2887.
- [14] H. Cui, L. Ma, Z. Huang, Z. Chen, C. Zhi, *SmartMat* **2022**, *3*, 565.
- [15] T. Lv, Y. Peng, G. Zhang, S. Jiang, Z. Yang, S. Yang, H. Pang, *Adv. Sci.* **2023**, *10*, 2206907.
- [16] T. Zhou, L. Zhu, L. Xie, Q. Han, X. Yang, L. Chen, G. Wang, X. Cao, *J. Colloid Interface Sci.* **2022**, *605*, 828.
- [17] B. Wan, Y. Wang, X. Chen, C. Zhan, H. Jiang, J.-H. Liu, Y. Gao, X. Jiang, X. Cao, H. Zhang, S.-X. Dou, Y. Xiao, *Chem. Sci.* **2025**, *16*, 8217.
- [18] Y. Liu, P. Hu, H. Liu, X. Wu, C. Zhi, *Mater. Today Energy* **2020**, *17*, 100431.
- [19] B. Aydogdu, S. Aydin, S. P. Sasikala, H. E. Unalan, S. O. Kim, R. Yuksel, *J. Energy Storage* **2024**, *86*, 111264.
- [20] X. Gu, J. Wang, X. Zhao, X. Jin, Y. Jiang, P. Dai, N. Wang, Z. Bai, M. Zhang, M. Wu, *J. Energy Chem.* **2023**, *85*, 30.
- [21] D. Zhang, Y. Yue, C. Yang, W. Limphirat, X. Zhang, J. Qin, J. Cao, *J. Chem. Eng.* **2025**, *506*, 160160.
- [22] W. Deng, C. Li, W. Zou, Y. Xu, Y. Chen, R. Li, *Small* **2024**, *20*, 2309527.
- [23] S. R. Popuri, M. Miclau, A. Artemenko, C. Labrugere, A. Villesuzanne, M. Pollet, *Inorg. Chem.* **2013**, *52*, 4780.
- [24] F. J. Morin, *Phys. Rev. Lett.* **1959**, *3*, 34.
- [25] Y. Liu, A. Liu, X. Chai, Y. Yang, M. Lu, X. Bai, Y. Chen, Y. Zhang, *Adv. Electron. Mater.* **2024**, *10*, 2300699.
- [26] J. B. Goodenough, *J. Solid State Chem.* **1971**, *3*, 490.
- [27] X. Liu, Y. Ren, L. Zhang, S. Zhang, *Front. Chem.* **2019**, *7*, 421.
- [28] B. Sambandam, S. Kim, D. T. Pham, V. Mathew, J. Lee, S. Lee, V. Soundharajan, S. Kim, M. H. Alfaruqi, J.-Y. Hwang, J. Kim, *Energy Storage Mater.* **2021**, *35*, 47.
- [29] Q. Li, J. Lin, S. Shen, M. Yang, M. Chen, M. Yang, Y. Wang, J. Chen, H. Mi, C. He, P. Zhang, D. Ma, *Small* **2025**, *21*, 2500767.
- [30] S. Castro-Pardo, A. B. Puthirath, S. Fan, S. Saju, G. Yang, J. Nanda, R. Vajtai, M. Tang, P. M. Ajayan, *J. Mater. Chem. A* **2024**, *12*, 2738.
- [31] Q. Yang, Z. Zou, X. Wu, S. Li, Y. Zhang, *Batteries (Basel.)* **2019**, *5*, 46.
- [32] Y. Xue, L. Miao, T. Hasegawa, A. Okawa, S. Yoshino, H. Kato, M. Kakihana, S. Yin, *Appl. Surf. Sci.* **2024**, *657*, 159779.
- [33] Y. Wang, S. Zhang, Y. Zhang, F. Chu, L. Hou, C. Yuan, *Electrochim. Acta* **2024**, *475*, 143623.
- [34] G. Liu, Q. Zeng, S. Tian, X. Sun, D. Wang, Q. Wu, W. Wei, T. Wu, Y. Zhang, Y. Sheng, K. Tao, E. Xie, Z. Zhang, *Small* **2024**, *20*, 2307040.
- [35] Y. Gan, C. Wang, J. Li, J. Zheng, Z. Wu, L. Lv, P. Liang, H. Wan, J. Zhang, H. Wang, *Front. Chem.* **2022**, *9*, 828119.
- [36] B. Stahl, T. Bredow, *ChemPhysChem* **2021**, *22*, 1018.
- [37] X. Geng, T. Chang, J. Fan, Y. Wang, X. Wang, Y. Sun, P. Selvarajan, C. Liu, C.-H. Lin, X. Wang, *ACS Appl. Mater. Interfaces* **2022**, *14*, 19736.
- [38] S. Wu, S. Tian, B. Liu, H. Tao, X. Zhao, R. G. Palgrave, G. Sankar, I. P. Parkin, *Solar Energy Mater. Solar Cells* **2018**, *176*, 427.
- [39] B. Dong, N. Shen, C. Cao, Z. Chen, H. Luo, Y. Gao, *RSC Adv.* **2016**, *6*, 81559.
- [40] R.-K. Wang, H. Wang, Z.-Q. An, J.-S. He, C.-L. Zhang, G.-P. Pan, X. Li, *J. Appl. Phys.* **2019**, *17*, 125.
- [41] R. Zhang, Q. S. Fu, C. Y. Yin, C. L. Li, X. H. Chen, G. Y. Qian, C. L. Lu, S. L. Yuan, X. J. Zhao, H. Z. Tao, *Sci. Rep.* **2018**, *8*, 17093.
- [42] N. Suzuki, Y. Xue, T. Hasegawa, S. Yin, *Solar Energy Mater. Solar Cells* **2023**, *251*, 112105.
- [43] J. Mendialdua, R. Casanova, Y. Barbaux, *J. Electron Spectrosc. Relat. Phenom.* **1995**, *71*, 249.
- [44] A. Polo, M. V. Dozzi, I. Grigioni, C. Lhermitte, N. Plainpan, L. Moretti, G. Cerullo, K. Sivila, E. Sellli, *Solar RRL* **2022**, *6*, 2200349.
- [45] Y. Gao, H. Luo, Z. Zhang, L. Kang, Z. Chen, J. Du, M. Kanehira, C. Cao, *Nano Energy* **2012**, *1*, 221.
- [46] P. Hu, P. Hu, T. D. Vu, M. Li, S. Wang, Y. Ke, X. Zeng, L. Mai, Y. Long, *Chem. Rev.* **2023**, *123*, 4353.
- [47] M. Nakano, K. Shibuya, D. Okuyama, T. Hatano, S. Ono, M. Kawasaki, Y. Iwasa, Y. Tokura, *Nature* **2012**, *487*, 459.
- [48] W. Wang, B. Jiang, L. Hu, Z. Lin, J. Hou, S. Jiao, *J. Power Sources* **2014**, *250*, 181.
- [49] J. Zhang, K. Zhu, Z. Kong, D. Ji, P. Liang, J. Wang, K. Yan, J. Liu, *Nano Mater. Sci.* **2024**, <https://doi.org/10.1016/j.nanoms.2024.07.003>.
- [50] Y. Cai, F. Liu, Z. Luo, G. Fang, J. Zhou, A. Pan, S. Liang, *Energy Stor. Mater.* **2018**, *13*, 168.
- [51] D. Bin, W. Huo, Y. Yuan, J. Huang, Y. Liu, Y. Zhang, F. Dong, Y. Wang, Y. Xia, *Chem* **2020**, *6*, 968.
- [52] J. Kumankuma-Sarpong, W. Guo, Y. Fu, *Small Methods* **2021**, *5*, 2100544.
- [53] W. Li, C. Han, Q. Gu, S.-L. Chou, J.-Z. Wang, H.-K. Liu, S.-X. Dou, *Adv. Energy Mater.* **2020**, *10*, 2001852.
- [54] T. Chen, X. Zhu, X. Chen, Q. Zhang, Y. Li, W. Peng, F. Zhang, X. Fan, *J. Power Sources* **2020**, *477*, 228652.
- [55] J. Wu, Q. Kuang, K. Zhang, J. Feng, C. Huang, J. Li, Q. Fan, Y. Dong, Y. Zhao, *Energy Stor. Mater.* **2021**, *41*, 297.
- [56] Y. Liu, X. Wu, *Nano Energy* **2021**, *86*, 106124.
- [57] B. Sambandam, V. Soundharajan, S. Kim, M. H. Alfaruqi, J. Jo, S. Kim, V. Mathew, Y.-K. Sun, J. Kim, *J. Mater. Chem. A* **2018**, *6*, 3850.

- [58] S. Islam, M. H. Alfaruqi, D. Y. Putro, V. Soundharajan, B. Sambandam, J. Jo, S. Park, S. Lee, V. Mathew, J. Kim, *J. Mater. Chem. A.* **2019**, *7*, 20335.
- [59] S. Deng, H. Li, B. Chen, Z. Xu, Y. Jiang, C. Li, W. Xiao, X. Yan, *J. Chem. Eng.* **2023**, *452*, 139115.
- [60] T. A. Mellan, R. Grau-Crespo, *J. Chem. Phys.* **2012**, *137*, 15.
- [61] C. Ling, Q. Wang, X. Wang, Z. Zhao, Z. Wang, J. Li, Y. Zhao, H. Jin, *J. Phys. Chem. C.* **2021**, *125*, 5816.
- [62] J. Guo, J. Ming, Y. Lei, W. Zhang, C. Xia, Y. Cui, H. N. Alshareef, *ACS Energy Lett.* **2019**, *4*, 2776.

Manuscript received: September 7, 2025

Revised manuscript received: October 15, 2025

Version of record online:
